

Article

Activation of Peroxymonosulfate by Chrysotile to Degrade Dyes in Water: Performance Enhancement and Activation Mechanism

Ying Dai ^{1,2} , Qian Peng ^{1,2}, Kun Liu ^{1,2,*} , Xuekun Tang ^{1,2}, Muyang Zhou ^{1,2}, Kun Jiang ^{1,2} and Binnan Zhu ³

¹ School of Minerals Processing and Bioengineering, Central South University, Changsha 410083, China; yingdaiyeah@163.com (Y.D.); pengqianhn@163.com (Q.P.); txk0797@126.com (X.T.); csu-zmy@csu.edu.cn (M.Z.); 195611072@csu.edu.cn (K.J.)

² Hunan Key Laboratory of Mineral Materials and Application, Central South University, Changsha 410083, China

³ Nanjing Kelilin Environmental Protection Technology Co., Ltd., Nanjing 211200, China; eric_zhu_machining@163.com

* Correspondence: kliu@csu.edu.cn

Abstract: An environmentally friendly activation method of peroxymonosulfate (PMS) provides a promising advanced oxidation processes for the degradation of organic wastewater. In this article, chrysotile, extracted from asbestos tailings, was found to be a kind of one-off catalyst relying on hydroxyl groups to activate PMS. Furthermore, the activation performance of the chrysotile had been greatly improved by the mean of calcining at 850 °C (850CC). It is worth mentioning that 850CC could not only realize three effective cycles, but also the mineralization ratio of Rhodamine B (RhB) could be impressively higher than 60%. According to characterization results, it was discovered that the chrysotile had transformed into forsterite with a fibrous morphology after calcination at 850 °C due to the loss of hydroxyl groups and the recombination of silicon, oxygen and magnesium atoms. Besides, the main active species produced by 850CC activating PMS were singlet oxygen and sulfate radicals. Further studies uncovered that PMS was successfully activated by a large number of unsaturated coordination oxygen on 850CC surface, and the activation mechanism was further elucidated. This study provides a new route for the comprehensive utilization of chrysotile and a valuable strategy for the degradation of hazardous organic pollutants in wastewater by PMS activation.

Keywords: chrysotile; peroxymonosulfate; forsterite; Rhodamine B; singlet oxygen; sulfate radicals



Citation: Dai, Y.; Peng, Q.; Liu, K.; Tang, X.; Zhou, M.; Jiang, K.; Zhu, B. Activation of Peroxymonosulfate by Chrysotile to Degrade Dyes in Water: Performance Enhancement and Activation Mechanism. *Minerals* **2021**, *11*, 400. <https://doi.org/10.3390/min11040400>

Academic Editor: Ljudmilla Bokányi

Received: 26 February 2021

Accepted: 6 April 2021

Published: 10 April 2021

Publisher's Note: MDPI stays neutral with regard to jurisdictional claims in published maps and institutional affiliations.



Copyright: © 2021 by the authors. Licensee MDPI, Basel, Switzerland. This article is an open access article distributed under the terms and conditions of the Creative Commons Attribution (CC BY) license (<https://creativecommons.org/licenses/by/4.0/>).

1. Introduction

Peroxymonosulfate (PMS)-based advanced oxidation processes (AOPs) have received extensive attention in recent decades because they can achieve efficient degradation of organic pollutants through generating sulfate radicals ($\text{SO}_4^{\cdot-}$) with high redox potential (2.5–3.1 V vs. Normal Hydrogen Electrode (NHE)) and longer half-time (30–40 μs) [1–3]. Generally speaking, PMS can be activated by catalysts including transition metal ions (such as Co^{2+} , Ag^+ , Fe^{2+} , Mn^{2+} , etc. [4–7]), transition metal oxides (such as Fe_3O_4 [8,9], MnO_2 [10,11], etc.), non-metallic materials (such as nano-carbon materials [12], benzoquinones [13], boron [14], graphene [15], etc.), or by different energies including ultrasound [16], heat [17] and light [18–20]. However, massive energy inputs, high cost and the secondary pollution greatly limit its practical application [21]. Therefore, it is an urgent and essential task to simply prepare an eco-friendly, low-cost and efficient catalyst.

In recent years, novel catalytic materials based on natural minerals have gradually entered the field of vision. For example, Li et al. [22] used the kaolinite with abundant surface hydroxyl groups and structural hydroxyl groups as a catalyst to effectively activate PMS to quickly and efficiently degrade the pollutant atrazine. Diao et al. [23] proved that the pyrite could successfully activate PMS in conjunction with ultrasonic irradiation

for 2,4-dichlorophenol (2,4-DCP) degradation in water. Huang et al. [24] used a simple hydrothermal method to load nano- α - MnO_2 on natural mineral palygorskite, and obtained α - MnO_2 /palygorskite composite material to degrade RhB. In addition, there were also many minerals used for PMS activation such as hematite [25], copper sulfide [26], etc. These studies show that natural minerals have great potential in the field of PMS activation.

It is worth noting that there are a lot of useful minerals in many tailings, which may be used as catalysts to activate PMS. Asbestos tailings, a typically hazardous solid waste produced during the mining and beneficiation of chrysotile (fibrid asbestos), contains a lot of tiny fibers and short fiber bundles of chrysotile which cannot be used by traditional technology [27]. If the chrysotile in tailings can be effectively used, the cost of catalysts will be significantly reduced. Herein, it is firstly reported that chrysotile extracted from asbestos tailings is simply calcined to prepare a PMS catalyst with high activity, excellent recycling performance and environmental friendliness. It is found that the raw chrysotile is a one-off catalyst depending on the surface hydroxyl groups, while the calcined chrysotile at 850 °C becomes a high-performance catalyst relying on the unsaturated coordinated O on the surface to activate PMS. This study provides a new route for the comprehensive utilization of chrysotile, and contributes an effective green catalyst for wastewater treatment.

2. Experimental

2.1. Materials and Chemical Reagents

The asbestos tailings used in this study were obtained from the Qilian asbestos mine, Qinghai Province, China. The chrysotile was carefully extracted and purified from the asbestos tailings by hand picking, gravity concentration and magnetic separation in the laboratory, resultantly, a high-purity chrysotile sample was obtained, as shown in Figure S1 and Table S1. Potassium peroxydisulfate (PMS, $\text{KHSO}_5 \cdot 0.5\text{KHSO}_4 \cdot 0.5\text{K}_2\text{SO}_4$, 95%) was purchased from Aladdin Bio-Chem Technology Co., Ltd. (Shanghai, China). Tert-butanol (TBA), methanol (MA), P-benzoquinone (p-BZ), L-Histidine (LH), hydrochloric acid (HCl, 36.5%), NaOH, 5,5-Dimethyl-1-pyrrolidine N-oxide (DMPO), 2,2,6,6-tetramethyl-4-piperidone (TEMP), Rhodamine B (RhB), Methylene blue (MB), Methyl orange (MO), Malachite Green (MG) and Acid Red 73 (AR 73) were purchased from Sinopharm Chemical Reagent Co., Ltd. (Shanghai, China). All chemicals were of analytical grade and used as received without further purification. Deionized water ($>18 \text{ M}\Omega \cdot \text{cm}$) was used throughout this experiment.

2.2. Calcination Experiment

Briefly, the obtained raw chrysotile was calcined in a muffle furnace at different temperatures (100–950 °C), respectively, for 2 h with a heating rate of 5 °C/min. The resultant sample was named as XCC, where X represents the calcination temperature.

2.3. Characterizations

The X-ray diffraction (XRD) patterns were characterized by an X-ray diffractometer (Empyrean, Panalytical, The Netherlands) using Cu $\text{K}\alpha$ source. The X-Ray Fluorescence Spectrometer (XRF) (AxiosmaAX, Panalytical, The Netherlands) was used to measure the proportion of chemical component. Specific surface area and pore structures of samples were determined by the Brunauer–Emmett–Teller (BET) and Barrett–Joyner–Halenda (BJH) models on a surface area and porosity analyzer (ASAP 2460, Micromeritics, Norcross, GA, USA). The X-ray photoelectron spectroscopy (XPS) was recorded by an ultrahigh vacuum electron spectrometer (K-Alpha 1063, Thermo Fisher, Loughborough, UK) with a monochromatic Al $\text{K}\alpha$ source. The valence bonding and functional group were measured on a Fourier transform infrared spectroscopy (FTIR) (UV-2350, Shimadzu, Kyoto, Japan). The morphological images were analyzed by a scanning electron microscope (SEM) (MIRA3 XMU/XMH, TESCAN, Brno, Czech Republic) and a transmission electron microscope (TEM) (Tecnai G2 F20, FEI, Hillsboro, OR, USA). The zeta potential of samples was measured on a Zeta potential analyzer (Zetasizer Nano ZS, Worcestershire, UK). The ab-

sorbance of degradation solution was measured on a UV-Vis spectrophotometer (UV-2600, Shimadzu, Kyoto, Japan). A total organic carbon (TOC) analyzer (TOC-L, Shimadzu, Kyoto, Japan) was used to detect the TOC concentration of the degradation products. Thermogravimetric and differential thermal analysis (TG-DTA) were analyzed by a synchronous thermal analyzer (SDTQ600, TA Instruments, New Castle, DE, US) from room temperature to 1000 °C. The leaching elements in the reaction process were quantitatively analyzed by an inductively coupled plasma atomic emission spectroscopy (ICP-AES) (Optima 8300, PerkinElmer, Waltham, MA, USA). An electron paramagnetic resonance (EPR) spectrometer (A-300, Bruker, Karlsruhe, Germany) with TEMP or DMPO as a spin-trapping agent was carried out to record the EPR experiment results.

2.4. Catalytic Degradation Experiments

All experiments were performed in a 250 mL glass beaker containing 100 mL pollutant solution with a constant stirring rate at a specific temperature. The typical operation steps are as follows: Firstly, the specific quality catalyst was added into the beaker. The mixture was mechanically stirred for 30 min to reach an adsorption and desorption equilibrium between pollutants and catalyst. Secondly, the activation for RhB degradation was started by adding PMS. During the experiment, a solution sample was taken out with a syringe every ten minutes, and the sample was filtered with a 0.22 µm needle filter to remove the chrysotile, and the sample was immediately taken to measure the absorbance on spectrophotometer at wavelength of 554 nm. Under the same experimental steps, the effects of different systems, catalyst dosages, PMS dosages, pH values, reaction temperatures and initial RhB concentrations on the catalytic reaction were investigated.

For the cyclic performance test of catalyst, the filtered catalyst after degradation was collected and dried at 80 °C for further catalytic reaction cycle. The following steps were exactly the same as those in the first catalytic degradation experiment.

The degradation ratio can be calculated according to Equation (1):

$$\text{Degradation ratio (\%)} = (C_0 - C_t)/C_0 \times 100\%, \quad (1)$$

where C_0 is the initial concentration of RhB (mg/L), C_t is the RhB concentration at time t (mg/L) in the 850CC/PMS system.

3. Results and Discussion

3.1. Performance Evaluation of PMS Activation by Raw Chrysotile

The cationic dye of Rhodamine B (RhB) was used as simulated pollutant to investigate the catalytic performances of chrysotile, as shown in Figure 1. It can be obviously observed that the degradation degree of RhB in the absence of catalyst achieves only 40% after 60 min. Meanwhile, chrysotile is unable to degrade RhB without PMS, suggesting that the contribution of adsorption to RhB degradation is weak because of the relatively small specific surface area (31.5 m²/g) and the surface electrical property (Figure S2). On the contrary, 100% of the degradation efficiency of RhB can be attained within 60 min in the presence of chrysotile and PMS (Figure 1a), indicating that chrysotile can efficiently activate PMS to generate reactive active species. However, the degradation efficiency of RhB shows a dramatic decline after use (Figure 1b). As a result, chrysotile is a kind of one-off catalyst for PMS activation, which must be enhanced to meet the requirements of practical application.

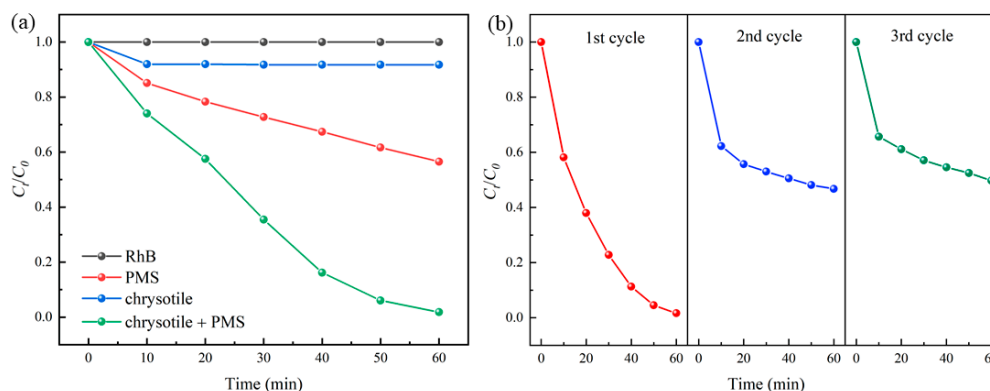


Figure 1. The degradation of RhB in the presence of chrysotile (a) and reusability of chrysotile (b). Control conditions: (PMS) = 1 mM, (chrysotile) = 1 g/L, (RhB) = 10 mg/L, temperature = 30 °C.

3.2. Performance Evaluation of PMS Activation by Calcined Chrysotile

As shown in Figure 2a, the chrysotile calcined at different temperatures was used to catalyze PMS for decomposing RhB. Obviously, the degradation effect remains unchanged when the calcination temperature is varied at the range of 0–400 °C. When continuing to increase the calcination temperature to 700 °C, the degradation efficiency decreases sharply. Interestingly, with the calcination temperature increased to 850 °C, complete degradation of RhB is restored. Over 850 °C, the degradation effect begins to decline.

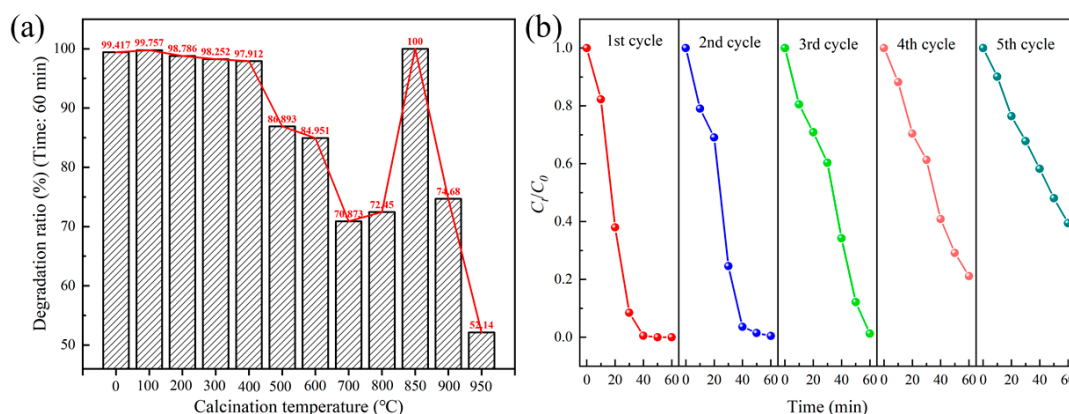


Figure 2. The degradation of RhB in the presence of PMS and chrysotile calcined at different temperatures (a) and reusability of 850CC (b). Control conditions: (PMS) = 1 mM, (XCC) = 1 g/L, (RhB) = 10 mg/L, temperature = 30 °C.

To clarify the cause of this phenomenon, TG-DTA was used to detect the thermal effects during the calcination process in 0–1000 °C with a heating rate of 10 °C/min in air atmosphere (Figure S3a). The chrysotile loses 5.5% of weight before 400 °C, and no endothermic peak is noticed during this process, which is attributed to evaporation of physically and chemically adsorbed water [28]. With the temperature increasing from 400 to 690 °C, the weight of chrysotile decreases quickly from 94.5% to 81%. Meanwhile, an obvious endothermic peak at 620 °C is observed, indicating the hydroxyl groups in the structure of chrysotile fall off [29]. Therefore, it is reasonable to speculate that the hydroxyl groups in chrysotile plays a dominant role in activating PMS to generate reactive species in chrysotile/PMS system. Furthermore, the functional groups of chrysotile calcined at different temperatures were characterized by FTIR, as depicted in Figure S3b. Bands at about 3600 and 1600 cm^{-1} are assigned to the stretching of hydroxyl groups and adsorbed water, respectively [30]. The peak intensity of hydroxyl groups and water molecules gradually decreases when the calcination temperature is increased to 700 °C, further verifying the primary role of hydroxyl groups on the surface of chrysotile in activating PMS

in chrysotile/PMS systems. Above 690 °C, weight loss is less than 2%. However, an obvious exothermic peak at 824 °C is found, which is due to the generation of new specie [31]. This means that the excellent performance of 850CC is related to the phase transition.

Figure 2b shows the reusability of 850CC. It can be observed that the degradation efficiency of RhB can still reach 100% after three cycles in the 850CC/PMS system. Obviously, 850CC has more excellent reusability than raw chrysotile (Figure S3c), indicating that calcination at 850 °C is an effective, simple and practicable strategy to enhance the catalytic performance of chrysotile. The enhancement mechanism will be described in detail in the following chapters. The result of TG-DTA proves that the temperature of 850 °C is enough to complete the phase change of chrysotile. Figure S3d describes the XRD patterns of chrysotile calcined under a series of temperatures. This result intuitively presents that forsterite is successfully obtained at 850 °C, which is consistent with previous studies [32].

3.3. Comparative Characterizations of 850CC and Raw Chrysotile

The chemical compositions of 850CC were detected by XRF, as shown in Table S1. The main element content of O, Si and Mg is more than 94% and impurity element content of Al, Fe and Ca is about 5%, which is similar to the raw chrysotile. The XRD patterns of 850CC and raw chrysotile are presented in Figure 3a. The diffraction peaks of 850CC are highly consistent with those of standard forsterite (JCPDS No. 99-0052), indicating the chrysotile phase is successfully transformed into forsterite at 850 °C.

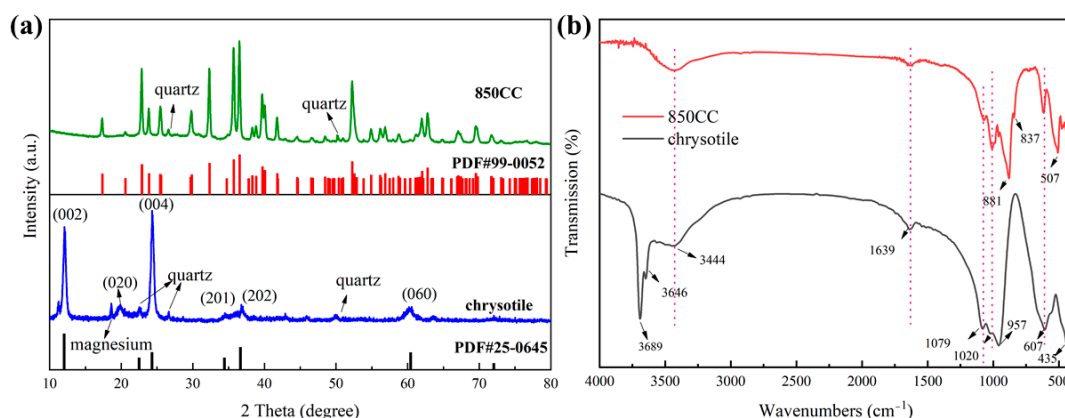


Figure 3. The XRD patterns (a) and FTIR spectra (b) of 850CC and raw chrysotile.

FTIR was employed to confirm the change in valence bonding and functional groups of 850CC and raw chrysotile (Figure 3b). In the FTIR spectrum of chrysotile, the obvious peaks at the 1079, 1020 and 957 cm^{-1} are indexed to the stretching vibration of Si-O-Si, Si-O-Mg and Si-O, respectively [33], indicating that the chrysotile structure is perfect. In the FTIR spectrum of 850CC, the characteristic peak of 1020 cm^{-1} disappears, and two new peaks appear at 881 and 837 cm^{-1} corresponding to Si-O-Si and Si-O stretching vibration of forsterite, which further confirms the formation of forsterite [34]. Bands at 3646 and 3689 cm^{-1} in the FTIR spectrum of chrysotile can be attributed to the vibration of the outer and inner hydroxyl groups of Mg-OH in the structure [35]. However, these bands are not detected in the FTIR spectrum of 850CC, which proves that there are no hydroxyl groups on the surface. Bands at 3444 and 1639 cm^{-1} in both FTIR spectra are due to the adsorption of water molecules in the air on the sample surface [31].

The morphology and microstructure of 850CC and raw chrysotile were investigated by SEM and TEM. As shown in Figure 4a, chrysotile has a fibrous appearance with an outer diameter of tens to hundreds of nanometers, and some fibers tightly gather together to form fiber bundles. 850CC, shown in Figure 4d, still remains fibrous in appearance and agglomerates tightly. Furthermore, it can be seen that the hollow tubular structure of raw chrysotile (Figure 4b,c) is destroyed during the calcination process, so 850CC presents a solid columnar structure (Figure 4e,f). The same conclusion can be drawn from the

BET analysis (Figure S4). The surface area and average pore size drastically decrease from $31.5 \text{ m}^2/\text{g}$ and 14.1 nm to $8.0 \text{ m}^2/\text{g}$ and 3.5 nm after $850 \text{ }^\circ\text{C}$ calcination, respectively. Comparing the pore size distribution of 850CC with raw chrysotile, it is found that the pores with pore size between 10 and 80 nm basically disappear. These results indicate that during the calcination, the loss of hydroxyl groups and the recombination of silicon, oxygen and magnesium atoms lead to the destruction of the hollow structure. In addition, the surface of 850CC is much rougher than that of raw chrysotile, and contains a lot of tiny particles with the size of about 10 nm , which indicates that some new interfaces are formed on the surface during the phase transition.

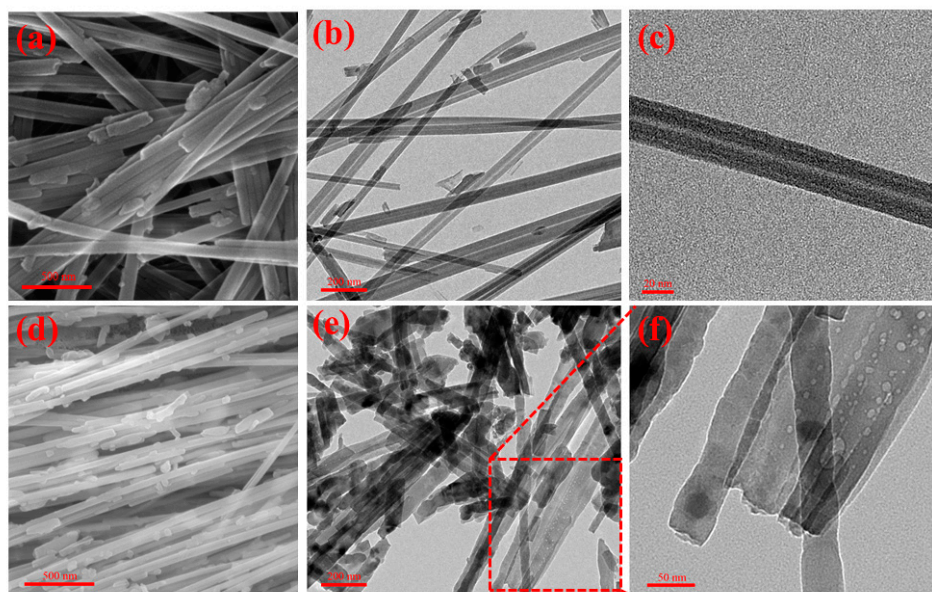


Figure 4. SEM and TEM images of raw chrysotile (a–c) and 850CC (d–f).

3.4. Effects of Various Parameters on the Degradation of RhB

To optimize the degradation process, the effects of PMS dosages, 850CC dosages, initial pH values, reaction temperatures and initial RhB concentrations on the degradation efficiency of RhB in 850CC/PMS were investigated in detail. Figure 5a presents the influence of PMS dosages, and the degradation efficiency gradually increases in the range of 0.5 – 2.5 mM , whereas a negative influence is observed in the case of overdose (in the range of 2.5 – 3 mM). This phenomenon can be explained by the fact that more reactive species will be produced as PMS dosage increases, and excessive PMS will cause the self-quenching effect of the reaction of $\text{SO}_4^{\cdot-}$ radicals and excessive $\text{HSO}_5^{\cdot-}$ [36]. Therefore, choosing the appropriate amount of PMS is extremely important. However, the amount with the best performance (2.5 mM) is not the most appropriate from the perspective of practical application. In the 850CC/PMS system, the RhB degradation ratio is not obviously improved when the amount of PMS increases from 1 mM to 2.5 mM . Hence, the follow-up experiments are conducted with 1.0 mM PMS based on the degradation results.

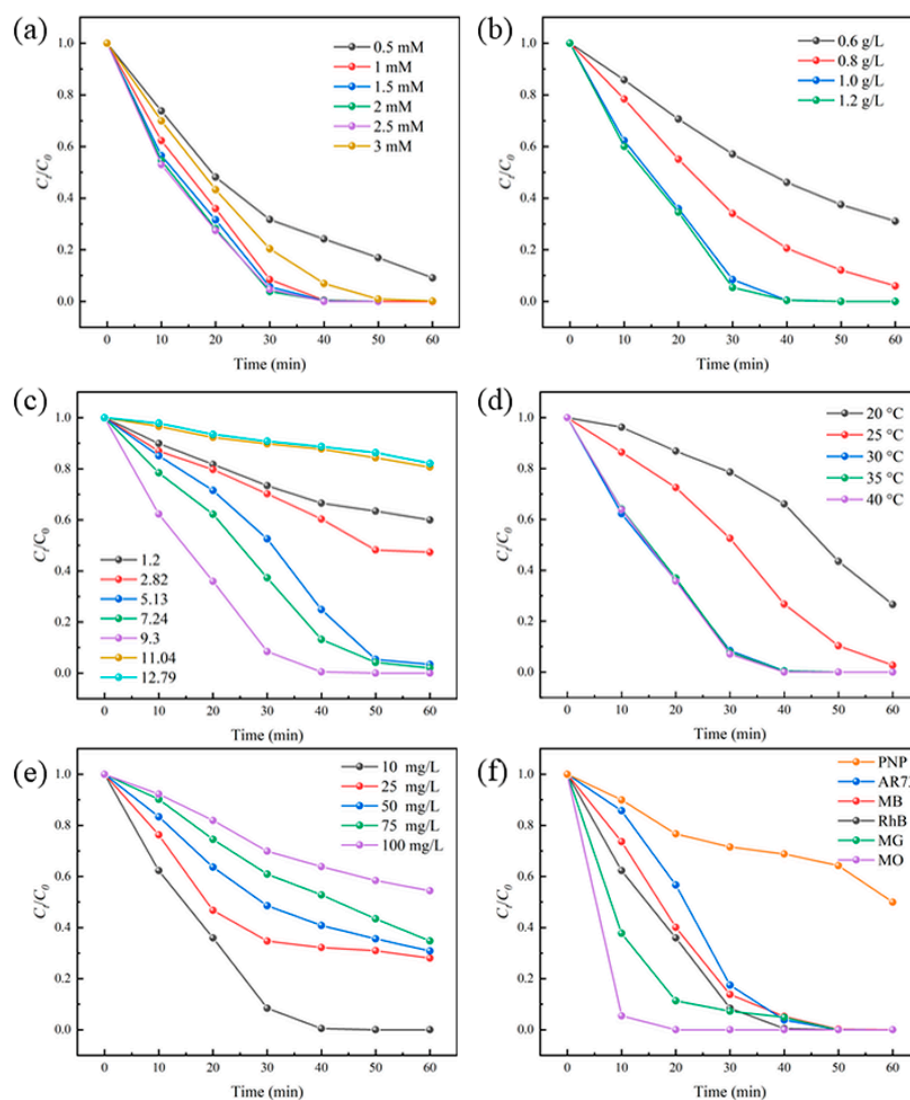


Figure 5. Effects of PMS dosages (a), catalyst dosages (b), initial pH values (c), reaction temperatures (d) and initial RhB concentrations (e) on the RhB degradation in the 850CC/PMS system, degradation effect of various dyes and PNP by 850CC/PMS (f). Control conditions: (RhB) = 10 mg/L, (850CC) = 1.0 g/L, (PMS) = 1.0 mM, temperature = 30 °C, (AR73) = (MB) = (MG) = (MO) = (PNP) = 10 mg/L.

The influence of 850CC dosages on the RhB degradation is displayed in Figure 5b. It can be seen that higher 850CC dosage results in better RhB degradation. This may be due to the fact that the higher catalyst loading can provide more active sites, thus facilitating the generation of more radicals from PMS.

The initial pH value plays a critical role in the RhB degradation since the pH value affects the surface potential of catalyst and the formation of organic compounds [37]. As shown in Figure 5c, the removal efficiency of RhB can reach close to 100% within 60 min in the range of pH 5.13–9.3, while decreases dramatically when the pH is lower than 5.13 or higher than 9.3. Because the zeta potential of 850CC is around 2.85 (Figure S2) and RhB is a cationic dye, the adsorption of RhB molecules on the surface of 850CC is inhibited when pH value is less than 2.85. Furthermore, in a strong acidic environment, H^+ can scavenge the generation of active oxygen species, resulting in a dramatic decrease in the degradation efficiency [38]. Besides, it is known that under strong alkaline condition, a lot of SO_5^{2-} are generated from PMS, which prevents the formation of $SO_4^{\cdot-}$ [39]. The degradation efficiency of 850CC/PMS decreases sharply when pH is higher than 11.04,

which indicates that $\text{SO}_4^{\cdot-}$ may be the main active species in the degradation process. Meanwhile, the agglomerates formed by the reaction of RhB with hydroxide are more difficult to be degraded [40]. Thus, the pH value from weak acidic to weak alkaline ($5.13 \leq \text{pH} \leq 9.3$) is an optimal environment for the reaction system.

Figure 5d shows the effect of the reaction temperature on the degradation of RhB. It can be seen that a degradation ratio of 100% is obtained within 60 min when the reaction temperature exceeds 25 °C, and the same degradation curve is obtained when the temperature is between 30 and 40 °C. Therefore, 30 °C is considered as a suitable reaction temperature.

The influence of initial RhB concentration is presented in Figure 5e. The degradation ratio gradually decreases from 100% to 40% when the initial RhB concentration increases from 10 mg/L to 100 mg/L. It demonstrates that the higher RhB concentration results in the lower degradation ratio. This can be attributed to the fact that large amounts of dye molecules and intermediates generated in the high RhB concentration solution are adsorbed on the surface of the 850CC, which impedes the intimate contact between PMS and active sites of the surface. Nonetheless, even 63% of RhB can be removed at an initial concentration of 50 mg/L and the removal ratio still reaches about 40% at the initial concentration of 100 mg/L, and the complete degradation of RhB still can be achieved by extending reaction time, which suggests that 850CC is an outstanding catalyst for PMS activation.

In order to probe the universality of 850CC, a variety of representative organic dyes were selected for degradation experiments, including Methylene blue (MB), Methyl orange (MO), Acid Red 73 (AR 73), Malachite green (MG), and RhB, as shown in Figure 5f. Obviously, the 850CC/PMS system can treat both cationic dyes (RhB, MB and MG) and anionic dyes (MO and AR73), exhibiting excellent catalytic degradation performances. Besides, P-nitrophenol (PNP), a common organic recalcitrant industrial pollutant, was also selected for degradation experiments. As seen in Figure 5f, about 50% of PNP can be degraded within 60 min, and the complete degradation still can be achieved by extending reaction time. The results indicate that 850CC can degrade not only dyes efficiently, but also industrial pollutants. Figure 6 shows the UV–Vis spectra of RhB solution during the degradation process in the 850CC/PMS system. It can be seen that, with the increase of reaction time, the absorbance intensity decreases and the peak does not shift, which means effective degradation of RhB. TOC analysis further confirms this conclusion by presenting a continuously increasing TOC removal ratio and a final mineralization ratio of near 62.6% (inset in Figure 6). This indicates that RhB in the 850CC/PMS system is not simple decolorization, but effect decomposition.

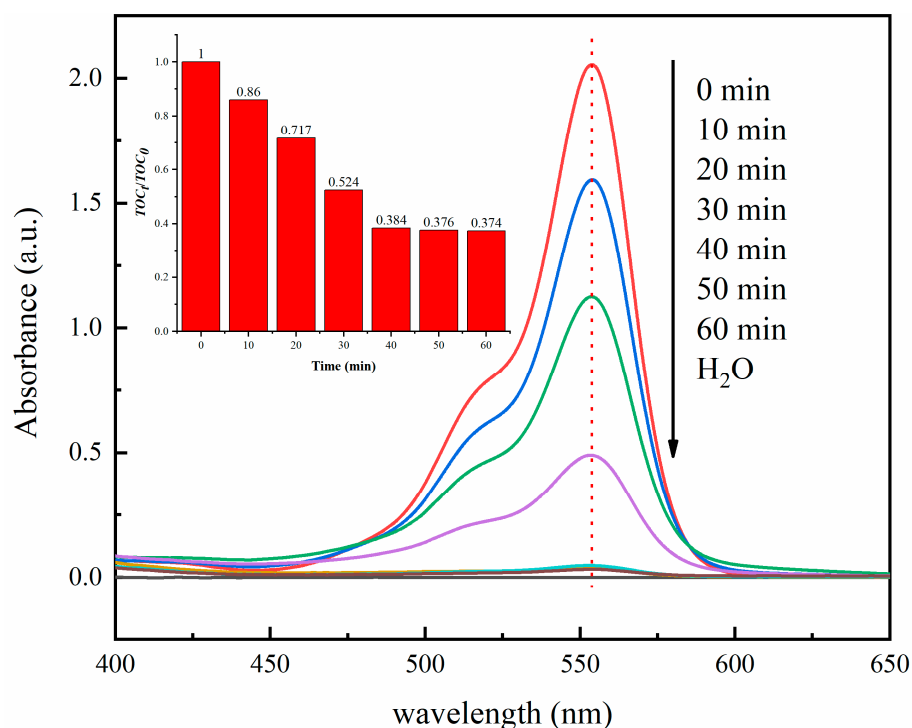


Figure 6. UV-Vis spectra of RhB solution during degradation process (the insert shows corresponding ratio of (TOC_t/TOC_0)).

3.5. Determination of Active Species

To confirm the reactive active species participated in the catalytic process in 850CC/PMS system, scavenging experiments were performed. The selectivity of the scavenger depends on the reaction rate between the scavenger and free radicals. According to previous studies, methanol (MA) was selected as a quencher for both hydroxyl radicals ($\cdot\text{OH}$) and sulfate radical ($\text{SO}_4^{\cdot-}$), and tert-butyl alcohol (TBA) was applied as an effective quencher for OH [41,42]. P-benzoquinone (p-BZ) has frequently served as an effective scavenger for superoxide anion radical ($\text{O}_2^{\cdot-}$) [43]. Even so, p-BZ is also reactive with $\cdot\text{OH}$ and $\text{SO}_4^{\cdot-}$ [44]. Zhou et al. [13] proved that p-BZ will be directly reactive with PMS under alkaline conditions. However, the pH value of the catalytic process in the 850CC/PMS system is lower than 7, so the consumption of PMS by p-BZ can be ignored. In addition, L-Histidine (LH) and furfuryl alcohol (FFA) have widely served as effective scavengers for singlet oxygen ($^1\text{O}_2$) ($K_1(\text{LH}, ^1\text{O}_2) = 2 \times 10^9 \text{ M}^{-1}\cdot\text{s}^{-1}$, $K_2(\text{FFA}, ^1\text{O}_2) = 1.2 \times 10^8 \text{ M}^{-1}\cdot\text{s}^{-1}$) [45,46]. Solís et al. [15] proposed that the consumption of PMS is accelerated in the presence of these scavengers following the order $\text{LH} > \text{FFA}$, indicating that FFA is more suitable as a chemical indicator for $^1\text{O}_2$ than LH. Yang et al. [47] verified that the reactions between FFA and PMS are highly sensitive to pH, and the ratio for PMS loss is lower than 5% when the reactions were carried out at pH 6. Therefore, it is reasonable that FFA is an effective scavenger for $^1\text{O}_2$ in this study.

As shown in Figure 7a and Figure S5, 100% of RhB is degraded in the absence of scavengers. The degradation efficiency reduces to 96% and 10% after the addition of MA and FFA, respectively, while it remains almost unchanged after adding TBA or p-BZ, indicating that $\text{SO}_4^{\cdot-}$ and $^1\text{O}_2$ are the reactive active species for pollutant degradation in the 850CC/PMS system. These results reveal that radical and non-radical paths are involved in the degradation of RhB and the latter takes over the leading factor. By the way, the reaction ratio decreases obviously in the presence of p-BZ, suggesting that $\text{O}_2^{\cdot-}$ participates in the degradation reaction of RhB, although it is not the main active species.

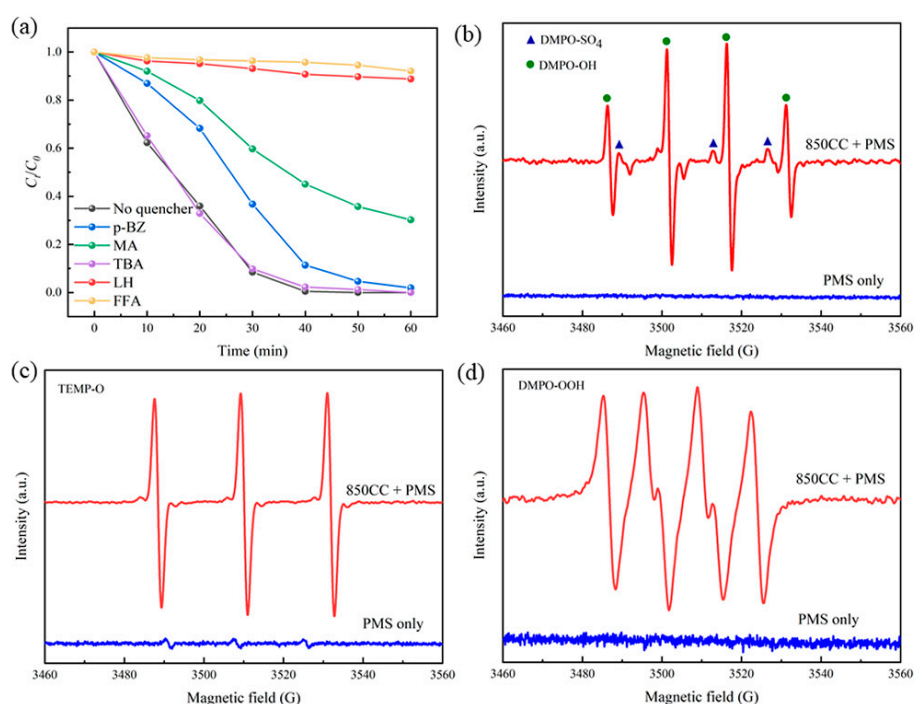


Figure 7. Effects of the radical scavengers on RhB degradation in the 850CC/PMS system (a) and EPR spectra of trapped radical adducts in different systems (b–d).

To intuitively detect the existence radicals, EPR was carried out with DMPO and TEMP as the radical spin trapping agents to identify $\text{SO}_4^{\cdot-}$, OH , $\text{O}_2^{\cdot-}$ and $^1\text{O}_2$ according to the formation of spin-adducts DMPO-SO₄, DMPO-OH, DMPO-OOH and TEMP-O, respectively [48,49]. As shown in Figure 7b, no signal is observed with DMPO in the absence of 850CC, indicating that $\text{SO}_4^{\cdot-}$ and $\cdot\text{OH}$ are not generated or below the detection limit without an efficient catalyst. In contrast, the standard characteristic peaks of DMPO-OH and DMPO-SO₄ adducts are detected in the 850CC/PMS-aqueous system, pointing out that there are $\text{SO}_4^{\cdot-}$ and OH in the system. The generation of two free radicals is mainly due to the reduction of PMS by the electrons in the uncoordinated oxygen on the surface of 850CC [50]. In addition, the standard characteristic peaks of TEMP-O (Figure 7c) and DMPO-OOH (Figure 7d) are detected, proving the existence of $\text{O}_2^{\cdot-}$ and $^1\text{O}_2$ in the 850CC/PMS system. Interestingly, in Figure 7c, the subtle triplet peaks are observed without addition of 850CC, which originates from the self-decomposition of PMS. The results of EPR and quenching experiments are mutually verified, further confirming the generation of reactive species and the key role of $^1\text{O}_2$ in the 850CC/PMS system.

3.6. Catalysis Mechanism

Firstly, the influence of various impurities on the catalytic degradation needs to be eliminated. As shown in Table S1, the major elements of 850CC are O, Si and Mg, which account for 93.74% of the overall composition. Ca and Fe are the main impurities, accounting for about 5%. In order to exclude the activation effect of MgO on PMS in the chrysotile, MgO with the same content as that in chrysotile was taken to activate PMS. As seen in Figure 8, the catalytic activity of MgO on PMS was negligible. Moreover, the results of ICP show that leaching concentration of Ca^{2+} and Fe^{3+} are 8.26 and 0.98 mg/L in the 850CC/PMS system. According to the literature, Ca and Fe in asbestos tailings exist primarily in the forms of CaO and Fe₂O₃, respectively [51]. To exclude the possible contribution of CaO and Fe₂O₃ to PMS activation, CaO/PMS and Fe₂O₃/PMS were employed to degrade RhB, as depicted in Figure 8. It can be found that over 50% of RhB at 60 min is degraded in the CaO/PMS system, while less than 40% in the Fe₂O₃/PMS system, suggesting the negligible effect of impurities towards the degradation system. The phenomenon of the slightly

better degradation in the CaO/PMS system can be explained as the activation of alkali [52]. Furthermore, to eliminate the co-catalysis of leached Fe^{3+} , 850CC/PMS with an additional 1.1 mg/L Fe^{3+} was used to degrade RhB. As seen in Figure 8, the addition of Fe^{3+} does not enhance the activation performance of 850CC, indicating that Fe^{3+} in the reaction solution is not responsible for the degradation of RhB. Moreover, the dissolution concentration of Mg^{2+} of 850CC during the catalytic process is determined by ICP as 16.6 mg/L; it has been proven by previous reports that Mg^{2+} does not have the ability to activate PMS [53]. Therefore, the catalysis reaction process of 850CC/PMS is heterogeneous.

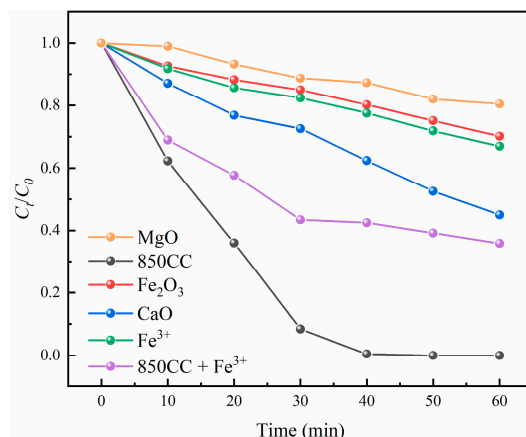


Figure 8. Degradation of RhB in CaO/PMS, Fe_2O_3 /PMS, homogeneous Fe^{3+} /PMS and 850CC/PMS with additional Fe^{3+} . Control conditions: (PMS) = 1 mM, (MgO) = 300 mg/L, (Fe_2O_3) = 35 mg/L, (Fe^{3+}) = 1.1 mg/L, (CaO) = 30 mg/L, temperature = 30 °C.

It has been confirmed that 850CC has better catalytic ability and cycle performance toward PMS than the chrysotile. However, as the number of cycles increases, the catalytic performance of 850CC gradually decreases. XPS was used to analyze the chemical changes of the catalysts before and after the degradation process. There is almost no change in all Mg 1s and Si 2p spectra. Figure 9 depicts the results of O 1s spectra of XPS of chrysotile and 850CC. For chrysotile, after reaction, the binding energy values of surface hydroxyls and lattice oxygen (O_2^-) in the MgO decreases 0.15 and 0.3 eV, respectively, indicating that OH^- and O_2^- participate in the reaction. The lost catalytic ability of used chrysotile may be resulted from the decreased intensity of surface hydroxyls, further suggesting that surface Mg-OH in chrysotile plays a dominant role in activating PMS. Meanwhile, the O 1s peak of fresh 850CC can be deconvoluted into two components, which can be assigned to the hydroxide (OH^-) in the surface hydroxyls (~531.8 eV) and the lattice oxygen (O_2^-) in the MgO (~530.9 eV) [54]. The former may be caused by the adsorption of water molecules on the catalyst surface [55]. After the reaction, the binding energy values in used 850CC remain unchanged, indicating that OH^- and O_2^- are not involved in the activation of PMS. The changes of peak intensity of OH^- and O_2^- are related to the adsorption of H_2O molecules and leaching of Mg^{2+} . Consequently, it is bound to exist another active site for activating PMS in the surface of 850CC.

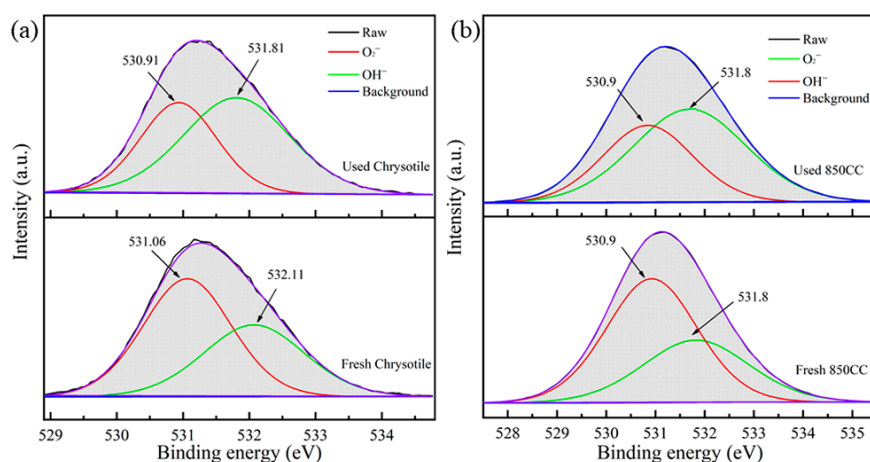


Figure 9. XPS spectra of O 1s for chrysotile (a) and 850CC (b) before and after catalytic degradation.

According to the XRD patterns (Figure S3d), it can be found that the sample is transformed into the forsterite phase when the calcination temperature exceeds 700 °C. Meanwhile, the activation performance of 700CC and 800CC is far less than that of 850CC (Figure 2). The temperature of 700 or 800 °C cannot meet the requirement of perfect phase transformation of chrysotile [32], which creates a negative effect on the formation of active sites on the sample surface. In addition, the degradation ratio decreases sharply when the calcination temperature is equal to or more than 900 °C. The crystallinity of samples can be calculated from the XRD patterns of Figure S3d [56], the crystallinity of 850CC (91.73%) is higher than that of 700CC (38.26%) and 800CC (88.54%), but obviously lower than that of 900CC (96.12%) and 950CC (97.94%). It can be concluded that the PMS activation property of calcined chrysotile is related to the surface properties and crystallinity of forsterite.

For the purpose of comparison, natural forsterite was used to catalyze PMS to degrade RhB, as shown in Figure 10a. It can be observed that natural forsterite cannot effectively activate PMS for RhB degradation. The SEM image and XRD pattern of nature forsterite (Figure S6) exhibit a typical granular morphology and excellent crystallinity (99.12%, more than all forsterites formed from chrysotile). The nano-fibrous appearance and proper crystallinity of 850CC endow it a higher specific surface area and more active sites, thus presenting an excellent catalytic performance.

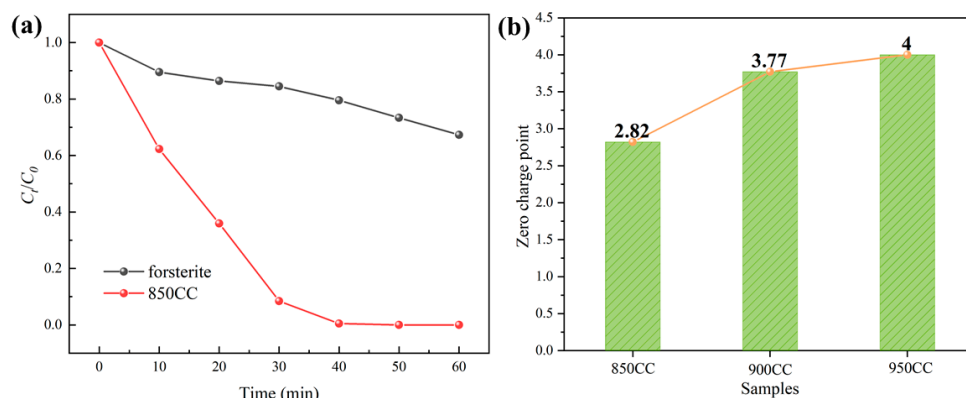
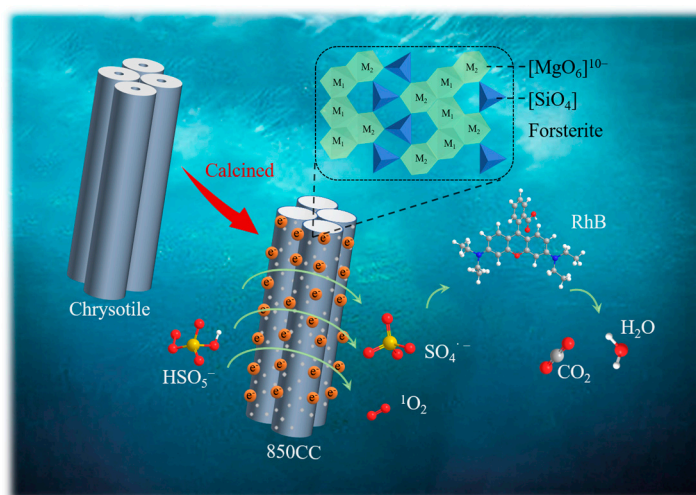


Figure 10. The comparison of catalytic performance between 850CC and natural forsterite (a) and point of zero charge of 850CC, 900CC and 950CC (b).

Comparing the element composition of 850CC with natural forsterite (Table S1), it can be found that the molar ratio of Mg to Si of 850CC (1.11) is markedly lower than that of natural forsterite (1.77). Forsterite is a dense orthosilicate of tetrahedral silicate and magnesium cation with a molar ratio of 1:2 [57]; the Mg^{2+} occupies two different octahedral

sites, in which one site shares edges and corners with $[\text{MgO}_6]^{10-}$ while another shares only corners [58]. As for 850CC, a large number of magnesium-oxygen octahedrons are not formed during the phase transition due to the lack of Mg atoms, which results in unsaturated silicon-oxygen tetrahedra and coordination oxygen. It has been confirmed that the increased unsaturated coordination oxygen on the surface reduces the positive charges [59]. Thus, the surface potential can be used to indirectly characterize the degree of unsaturated coordination oxygen on the sample surface. As shown in Figure S2, the point of zero charge of 850CC is 2.8, which is obviously lower than that of natural forsterite ($\text{pH}_{\text{zpc}} = 4.1$) [60,61], proving the existence of a large amount of unsaturated coordination oxygen on the surface. Interestingly, it is obviously observed that the increased point of zero charge can be obtained when the calcination temperature is increased (Figure 10b), which indicates that higher calcination temperature leads to higher crystallinity, and thus reduces the amount of unsaturated coordination oxygen.

Therefore, it is reasonable to think that the catalytic performance of calcined chrysotile is closely related to its unsaturated coordination oxygen. With the increase of calcination temperature, the crystal structure of forsterite will continue to adjust, and the unsaturated coordination oxygen will gradually decrease until it finally transforms into enstatite with the molar ratio of Mg to Si of 1:1 [62]. As a result, it can be concluded that the appropriate crystallinity and a large amount of unsaturated coordination oxygen of 850CC play key roles in activating PMS to degrade dyes. The possible catalytic pathways are proposed, as shown in Scheme 1. Briefly, PMS (i.e., HSO_5^-) is attached to the unsaturated coordination oxygen on forsterite via chemical bonds to form forsterite-(OH)OSO $_3^-$ complex, which further decomposes into an intermediate with the release of the sulfate moiety through intramolecular nucleophilic displacement with other unsaturated coordination oxygen at the O–O bond [22,63]. Then, the generated intermediate is attacked by two ionized PMS ions (SO_5^{2-}) to produce $^1\text{O}_2$ [13,64]. Additionally, electron transfer inside forsterite-(OH)OSO $_3^-$ complex leads to the generation of $\text{SO}_4^{\cdot-}$ and OH [65]. Finally, $^1\text{O}_2$ and $\text{SO}_4^{\cdot-}$ can attack the RhB molecule with the formation of transformation products, which are eventually mineralized into CO_2 and H_2O .



Scheme 1. Proposed PMS activation mechanism over 850CC in degradation of RhB.

3.7. Effects of Inorganic Ions and NOM on the Degradation of RhB

Inorganic anions and natural organic matter (NOM) are widely presented at various concentrations in real wastewaters. For this reason, the effect of selected anions (Cl^- , NO_3^- , HCO_3^- , CO_3^{2-} and H_2PO_4^-) and humic acid (HA) as potentially interfering substances on the degradation of RhB was investigated, as illustrated in Figure 11. It can be seen that HCO_3^- or CO_3^{2-} exhibits extreme adverse effects on RhB degradation, while NO_3^- and H_2PO_4^- cause mild inhibition of RhB degradation. Especially, the degradation of

RhB in the 850CC/PMS system is extremely enhanced at the present of Cl^- . According to previous reports, Cl^- could be directly oxidized through two-electron transfer in a Cl^-/PMS system, thereby producing reactive chlorine species (Cl_2/HClO) [66–68]. Usually, NO_3^- , HCO_3^- , CO_3^{2-} and H_2PO_4^- can scavenge free radicals such as $\text{SO}_4^{\cdot-}$ and $\cdot\text{OH}$, leading to a decrease in degradation [69,70]. In a 850CC/PMS system, a negligible reduction in degradation ratio of RhB is observed in the presence of NO_3^- or H_2PO_4^- . The above results have proved that RhB degradation in the 850CC/PMS system proceeds in a $^1\text{O}_2$ -dominated non-radical manner. The obvious reduction of degradation is observed when the HCO_3^- or CO_3^{2-} is added into the reaction system, and the pH values after addition were 10.02 and 10.53, respectively. This result indicates that the increased alkalinity is the cause of this phenomenon, as discussed above. In addition, the addition of 20 mg/L of humic acids (HA) decreases the degradation effect, because HA may react with radical species [71].

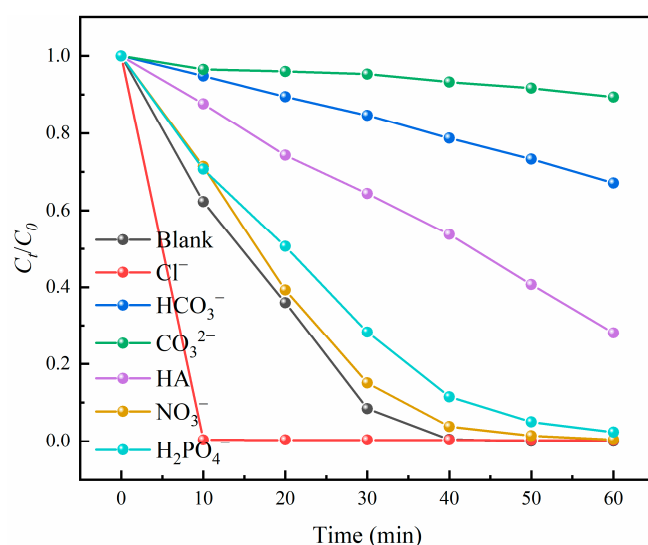


Figure 11. Effect of co-existing anions and HA on RhB degradation. Control condition: (850CC) = 1.0 g/L, (PMS) = 1.0 mM, temperature = 30 °C, (Cl^-) = (NO_3^-) = (HCO_3^-) = (CO_3^{2-}) = (H_2PO_4^-) = 0.2 M, (HA) = 20 mg/L.

4. Conclusions

In a nutshell, the nature chrysotile is discovered to be a kind of one-off catalyst for PMS activation, while the obtained 850CC by calcination has better catalytic degradation performance and reusability. The 850CC still retains the chrysotile-like morphology, and possesses a large number of defects on its surface. Impressively, systematic studies have certified that the active site of 850CC is the unsaturated coordination oxygen on the surface, and the main active species produced in PMS activation are singlet oxygen and sulfate radicals. In addition, in the 850CC/PMS system, not only a mineralization ratio of RhB can reach more than 60%, but also a variety of other dyes can be effectively degraded. Overall, calcined chrysotile is a promising PMS activator, which can effectively remove organic pollutants in water and improve the utilization of asbestos tailings.

Supplementary Materials: The following are available online at <https://www.mdpi.com/article/10.3390/min11040400/s1>: Figure S1. The XRD pattern of raw chrysotile from asbestos tailings, Figure S2. The Zeta potentials and points of zero charge of 850CC and raw chrysotile, Figure S3. The TG-DTA curves of chrysotile (a), FTIR spectra (b) and XRD patterns (d) of chrysotile with different calcination temperatures, and comparison of reusability between 850CC and raw chrysotile (c), Figure S4. Nitrogen isotherm adsorption-desorption curves (a) and pore size distribution curves (b) of raw chrysotile and 850CC, Figure S5. Effects of the radical scavengers on RhB degradation in 850CC/PMS system: TBA (a), MA (b), p-BZ (c) and LH (d), Figure S6. The SEM images (a) and XRD

patterns of forsterite (b), Table S1. The element composition of raw chrysotile, 850CC and natural forsterite.

Author Contributions: Formal analysis, Y.D.; investigation, X.T. and K.J.; methodology, M.Z.; resources, B.Z.; writing—original draft, Y.D.; writing—review and editing, Q.P. and K.L. All authors have read and agreed to the published version of the manuscript.

Funding: National Natural Science Foundation of China, No. 51774330; Fundamental Research Funds for Central Universities of the Central South University, No. 2020zzts736.

Institutional Review Board Statement: Not applicable.

Informed Consent Statement: Not applicable.

Data Availability Statement: Not applicable.

Acknowledgments: This work was supported by the National Natural Science Foundation of China (No. 51774330) and the Fundamental Research Funds for the Central Universities of Central South University (No. 2020zzts736).

Conflicts of Interest: The authors declare no conflict of interest.

References

1. Dionysiou, D.D. Degradation of Organic Contaminants in Water with Sulfate Radicals Generated by the Conjunction of Peroxymonosulfate with Cobalt. *Environ. Sci. Technol.* **2003**, *37*, 4790–4797. [[CrossRef](#)]
2. Wang, C.; Kim, J.; Kim, M.; Lim, H.; Zhang, M.; You, J.; Yun, J.H.; Bando, Y.; Li, J.; Yamauchi, Y. Nanoarchitected metal-organic framework-derived hollow carbon nanofiber filters for advanced oxidation processes. *J. Mater. Chem. A* **2019**, *7*, 13743–13750. [[CrossRef](#)]
3. Ji, Y.; Ferronato, C.; Salvador, A.; Yang, X.; Chovelon, J.M. Degradation of ciprofloxacin and sulfamethoxazole by ferrous-activated persulfate: Implications for remediation of groundwater contaminated by antibiotics. *Sci. Total Environ.* **2014**, *472*, 800–808. [[CrossRef](#)]
4. Anipsitakis, G.P.; Dionysiou, D.D. Radical generation by the interaction of transition metals with common oxidants. *Environ. Sci. Technol.* **2004**, *38*, 3705–3712. [[CrossRef](#)] [[PubMed](#)]
5. Hu, P.; Long, M. Cobalt-catalyzed sulfate radical-based advanced oxidation: A review on heterogeneous catalysts and applications. *Appl. Catal. B Environ.* **2016**, *181*, 103–117. [[CrossRef](#)]
6. Li, Z.; Tang, X.; Huang, G.; Luo, X.; He, D.; Peng, Q.; Huang, J.; Ao, M.; Liu, K. Bismuth MOFs based hierarchical $\text{Co}_3\text{O}_4\text{-Bi}_2\text{O}_3$ composite: An efficient heterogeneous peroxymonosulfate activator for azo dyes degradation. *Sep. Purif. Technol.* **2020**, *242*, 116825. [[CrossRef](#)]
7. Zhang, Y.; Zhang, B.T.; Teng, Y.; Zhao, J.; Kuang, L.; Sun, X. Carbon nanofibers supported Co/Ag bimetallic nanoparticles for heterogeneous activation of peroxymonosulfate and efficient oxidation of amoxicillin. *J. Hazard. Mater.* **2020**, *400*, 123290. [[CrossRef](#)] [[PubMed](#)]
8. Li, J.; Wan, Y.; Li, Y.; Yao, G.; Lai, B. Applied Catalysis B: Environmental Surface Fe (III)/Fe (II) cycle promoted the degradation of atrazine by peroxymonosulfate activation in the presence of hydroxylamine. *Appl. Catal. B Environ.* **2019**, *256*, 117782. [[CrossRef](#)]
9. Tang, X.; Huang, J.; Liu, K.; Feng, Q.; Li, Z.; Ao, M. Synthesis of magnetically separable $\text{MnO}_2/\text{Fe}_3\text{O}_4$ /silica nanofiber composite with enhanced Fenton-like catalytic activity for degradation of Acid Red 73. *Surf. Coat. Technol.* **2018**, *354*, 18–27. [[CrossRef](#)]
10. Wang, Y.; Sun, H.; Ang, H.M.; Tade, M.O.; Wang, S. 3D-hierarchically structured MnO_2 for catalytic oxidation of phenol solutions by activation of peroxymonosulfate: Structure dependence and mechanism. *Appl. Catal. B Environ.* **2015**, *164*, 159–167. [[CrossRef](#)]
11. Xu, Y.; Lin, H.; Li, Y.; Zhang, H. The mechanism and efficiency of MnO_2 activated persulfate process coupled with electrolysis. *Sci. Total Environ.* **2017**, *609*, 644–654. [[CrossRef](#)]
12. Peng, Q.; Dai, Y.; Liu, K.; Luo, X.; He, D.; Tang, X.; Huang, G. A novel carbon nanotube–magnesium oxide composite with excellent recyclability to efficiently activate peroxymonosulfate for Rhodamine B degradation. *J. Mater. Sci.* **2020**, *55*, 11267–11283. [[CrossRef](#)]
13. Zhou, Y.; Jiang, J.; Gao, Y.; Pang, S.; Li, J.; Lu, X.; Yuan, L. Activation of Peroxymonosulfate by Benzoquinone: A Novel Nonradical Oxidation Process. *Environ. Sci. Technol.* **2015**. [[CrossRef](#)] [[PubMed](#)]
14. Ren, W.; Zhou, P.; Nie, G.; Cheng, C.; Duan, X.; Zhang, H.; Wang, S. Hydroxyl radical dominated elimination of plasticizers by peroxymonosulfate on metal-free boron: Kinetics and mechanisms. *Water Res.* **2020**, *186*, 116361. [[CrossRef](#)] [[PubMed](#)]
15. Solís, R.R.; Mena, I.F.; Nadagouda, M.N.; Dionysiou, D.D. Adsorptive interaction of peroxymonosulfate with graphene and catalytic assessment via non-radical pathway for the removal of aqueous pharmaceuticals. *J. Hazard. Mater.* **2020**, *384*, 121340. [[CrossRef](#)] [[PubMed](#)]
16. Zeng, F.; Cao, S.; Jin, W.; Zhou, X.; Ding, W.; Tu, R.; Han, S.F.; Wang, C.; Jiang, Q.; Huang, H.; et al. Inactivation of chlorine-resistant bacterial spores in drinking water using UV irradiation, UV/Hydrogen peroxide and UV/Peroxymonosulfate: Efficiency and mechanism. *J. Clean. Prod.* **2020**, *243*, 118666. [[CrossRef](#)]

17. Norzaee, S.; Taghavi, M.; Djahed, B.; Kord Mostafapour, F. Degradation of Penicillin G by heat activated persulfate in aqueous solution. *J. Environ. Manag.* **2018**, *215*, 316–323. [[CrossRef](#)]
18. Huang, G.; Li, Z.; Liu, K.; Tang, X.; Huang, J.; Zhang, G. Bismuth MOF-derived BiOBr/Bi₂₄O₃₁Br₁₀ heterojunctions with enhanced visible-light photocatalytic performance. *Catal. Sci. Technol.* **2020**, *10*, 4645–4654. [[CrossRef](#)]
19. Solís, R.R.; Rivas, F.J.; Tierno, M. Monopersulfate photocatalysis under 365 nm radiation. Direct oxidation and monopersulfate promoted photocatalysis of the herbicide tembotrione. *J. Environ. Manag.* **2016**, *181*, 385–394. [[CrossRef](#)] [[PubMed](#)]
20. Solís, R.R.; Rivas, F.J.; Chávez, A.M.; Dionysiou, D.D. Peroxymonosulfate/solar radiation process for the removal of aqueous microcontaminants. Kinetic modeling, influence of variables and matrix constituents. *J. Hazard. Mater.* **2020**, *400*, 123118. [[CrossRef](#)] [[PubMed](#)]
21. Ghanbari, F.; Moradi, M. Application of peroxymonosulfate and its activation methods for degradation of environmental organic pollutants: Review. *Chem. Eng. J.* **2017**, *310*, 41–62. [[CrossRef](#)]
22. Nie, W.; Mao, Q.; Ding, Y.; Hu, Y.; Tang, H. Highly efficient catalysis of chalcopyrite with surface bonded ferrous species for activation of peroxymonosulfate toward degradation of bisphenol A: A mechanism study. *J. Hazard. Mater.* **2019**, *364*, 59–68. [[CrossRef](#)]
23. Diao, Z.H.; Lin, Z.Y.; Chen, X.Z.; Yan, L.; Dong, F.X.; Qian, W.; Kong, L.J.; Du, J.J.; Chu, W. Ultrasound-assisted heterogeneous activation of peroxymonosulphate by natural pyrite for 2,4-dichlorophenol degradation in water: Synergistic effects, pathway and mechanism. *Chem. Eng. J.* **2020**, *389*, 123771. [[CrossRef](#)]
24. Huang, C.; Wang, Y.; Gong, M.; Wang, W.; Mu, Y.; Hu, Z.H. A-MnO₂/Palygorskite composite as an effective catalyst for heterogeneous activation of peroxymonosulfate (PMS) for the degradation of Rhodamine B. *Sep. Purif. Technol.* **2020**, *230*, 115877. [[CrossRef](#)]
25. Yu, M.; Teel, A.L.; Watts, R.J. Activation of Peroxymonosulfate by Subsurface Minerals. *J. Contam. Hydrol.* **2016**, *191*, 33–43. [[CrossRef](#)] [[PubMed](#)]
26. Wang, X.; Ding, Y.; Dionysiou, D.D.; Liu, C.; Tong, Y.; Gao, J.; Fang, G.; Zhou, D. Efficient activation of peroxymonosulfate by copper sulfide for diethyl phthalate degradation: Performance, radical generation and mechanism. *Sci. Total Environ.* **2020**, *749*, 142387. [[CrossRef](#)] [[PubMed](#)]
27. Zheng, W.M.; Sun, H.J.; Peng, T.J.; Zeng, L. Thermal process and mechanism of phase transition and detoxification of glass-ceramics from asbestos tailings. *J. Non Cryst. Solids* **2019**, *517*, 26–31. [[CrossRef](#)]
28. Zhuravlev, L.T. The surface chemistry of amorphous silica. Zhuravlev model. *Colloids Surf. A Physicochem. Eng. Asp.* **2000**, *173*, 1–38. [[CrossRef](#)]
29. Wang, L.; Lu, A.; Wang, C.; Zheng, X.; Zhao, D.; Liu, R. Nano-fibriform production of silica from natural chrysotile. *J. Colloid Interface Sci.* **2006**, *295*, 436–439. [[CrossRef](#)] [[PubMed](#)]
30. Bing, W.; Wei, W. Degradation Phenol Wastewater by Heating Activated Persulfate. *Int. J. Environ. Monit. Anal.* **2019**, *7*, 14. [[CrossRef](#)]
31. Wypych, F.; Schreiner, W.H.; Richard, E. Grafting of phenylarsonic and 2-nitrophenol-4-arsonic acid onto disordered silica obtained by selective leaching of brucite-like sheet from chrysotile structure. *J. Colloid Interface Sci.* **2004**, *276*, 167–173. [[CrossRef](#)] [[PubMed](#)]
32. Kusiorowski, R.; Zaremba, T.; Piotrowski, J.; Adamek, J. Thermal decomposition of different types of asbestos. *J. Therm. Anal. Calorim.* **2012**, *109*, 693–704. [[CrossRef](#)]
33. Valouma, A.; Verganelaki, A.; Maravelaki-Kalaitzaki, P.; Gidarakos, E. Chrysotile asbestos detoxification with a combined treatment of oxalic acid and silicates producing amorphous silica and biomaterial. *J. Hazard. Mater.* **2016**, *305*, 164–170. [[CrossRef](#)] [[PubMed](#)]
34. Choudhary, R.; Venkatraman, S.K.; Bulygina, I.; Chatterjee, A.; Abraham, J.; Senatov, F.; Kaloshkin, S.; Ilyasov, A.; Abakumov, M.; Knyazeva, M.; et al. Impact of forsterite addition on mechanical and biological properties of composites. *J. Asian Ceram. Soc.* **2020**, *8*, 1051–1065. [[CrossRef](#)]
35. Giroto, C.P.; de Campos, S.D.; de Campos, É.A. Chrysotile asbestos treated with phosphoric acid as an adsorbent for ammonia nitrogen. *Heliyon* **2020**, *6*. [[CrossRef](#)] [[PubMed](#)]
36. Ben, S.; Zhao, F.; Safaei, Z.; Lakshamy, D. Sulfate radical-mediated degradation and mineralization of bisphenol F in neutral medium by the novel magnetic Sr₂CoFeO₆ double perovskite oxide catalyzed peroxymonosulfate: Influence of co-existing chemicals and UV irradiation. *Appl. Catal. B Environ.* **2018**, *233*, 99–111. [[CrossRef](#)]
37. Lin, H.; Zhang, H.; Hou, L. Degradation of c. i. acid orange 7 in aqueous solution by a novel electro/Fe₃O₄/pds process. *J. Hazard. Mater.* **2014**, *276*, 182–191. [[CrossRef](#)]
38. Guan, Y.; Ma, J.; Li, X.; Fang, J.; Chen, L. Influence of pH on the Formation of Sulfate and Hydroxyl Radicals in the UV / Peroxymonosulfate System. *Environ. Sci. Technol.* **2011**, *45*, 9308–9314. [[CrossRef](#)]
39. Yang, F.; Huang, Y.; Fang, C.; Xue, Y.; Ai, L.; Liu, J.; Wang, Z. Peroxymonosulfate/base process in saline wastewater treatment: The fight between alkalinity and chloride ions. *Chemosphere* **2018**, *199*, 84–88. [[CrossRef](#)]
40. Nookaraju, M.; Rajini, A.; Venkatathri, N.; Reddy, I.A.K. Catalytic degradation of rhodamine B over FeMCM-41. *Asian J. Chem.* **2012**, *24*, 5817–5820.
41. Oh, W.D.; Dong, Z.; Lim, T.T. Generation of sulfate radical through heterogeneous catalysis for organic contaminants removal: Current development, challenges and prospects. *Appl. Catal. B Environ.* **2016**, *194*, 169–201. [[CrossRef](#)]

42. Xu, H.; Wang, D.; Ma, J.; Zhang, T.; Lu, X.; Chen, Z. Applied Catalysis B: Environmental A superior active and stable spinel sulfide for catalytic peroxymonosulfate oxidation of bisphenol S. *Appl. Catal. B Environ.* **2018**, *238*, 557–567. [[CrossRef](#)]
43. Rao, P.S.; Hayon, E. Redox potentials of free radicals. IV. Superoxide and hydroperoxy radicals $\cdot\text{O}_2^-$ and $\cdot\text{HO}_2$. *J. Phys. Chem.* **1975**, *79*, 397–402. [[CrossRef](#)]
44. Schuchmann, M.N.; Bothe, E.; Sonntag, J.V.; Sonntag, C.V. Reaction of OH radicals with benzoquinone in aqueous solutions. a pulse radiolysis study. *J. Chem. Soc.* **1988**, *4*, 791–796. [[CrossRef](#)]
45. Yun, E.; Lee, J.H.; Kim, J.; Park, H.; Lee, J. Identifying the Nonradical Mechanism in the Peroxymonosulfate Activation Process: Singlet Oxygenation Versus Mediated Electron Transfer. *Environ. Sci. Technol.* **2018**, *52*, 7032–7042. [[CrossRef](#)] [[PubMed](#)]
46. Wu, S.; Liu, H.; Yang, C.; Li, X.; Lin, Y.; Yin, K.; Sun, J.; Teng, Q.; Du, C.; Zhong, Y. High-performance porous carbon catalysts doped by iron and nitrogen for degradation of bisphenol F via peroxymonosulfate activation. *Chem. Eng. J.* **2020**, *392*, 123683. [[CrossRef](#)]
47. Yang, Y.; Banerjee, G.; Brudvig, G.W.; Kim, J.H.; Pignatello, J.J. Oxidation of Organic Compounds in Water by Unactivated Peroxymonosulfate. *Environ. Sci. Technol.* **2018**, *52*, 5911–5919. [[CrossRef](#)] [[PubMed](#)]
48. Fontmorin, J.M.; Burgos Castillo, R.C.; Tang, W.Z.; Sillanpää, M. Stability of 5,5-dimethyl-1-pyrroline-N-oxide as a spin-trap for quantification of hydroxyl radicals in processes based on Fenton reaction. *Water Res.* **2016**, *99*, 24–32. [[CrossRef](#)] [[PubMed](#)]
49. Mendoza, C.; Désert, A.; Khrouz, L.; Pérez, C.A.; Parola, S.; Heinrichs, B. Heterogeneous singlet oxygen generation: In-operando visible light EPR spectroscopy. *Environ. Sci. Pollut. Res.* **2019**. [[CrossRef](#)] [[PubMed](#)]
50. Zhang, H.; Li, C.; Lyu, L.; Hu, C. Surface oxygen vacancy inducing peroxymonosulfate activation through electron donation of pollutants over cobalt-zinc ferrite for water purification. *Appl. Catal. B Environ.* **2020**, *270*, 118874. [[CrossRef](#)]
51. Leonelli, C.; Veronesi, P.; Boccaccini, D.N.; Rivasi, M.R.; Barbieri, L.; Andreola, F.; Lancellotti, I.; Rabitti, D.; Pellacani, G.C. Microwave thermal inertisation of asbestos containing waste and its recycling in traditional ceramics. *J. Hazard. Mater.* **2006**, *135*, 149–155. [[CrossRef](#)]
52. Qi, C.; Liu, X.; Ma, J.; Lin, C.; Li, X.; Zhang, H. Activation of peroxymonosulfate by base: Implications for the degradation of organic pollutants. *Chemosphere* **2016**, *151*, 280–288. [[CrossRef](#)]
53. Peng, Q.; Tang, X.; Liu, K.; Luo, X.; He, D.; Dai, Y.; Huang, G. High-efficiency catalysis of peroxymonosulfate by mgo for the degradation of organic pollutants. *Minerals* **2020**, *10*, 2. [[CrossRef](#)]
54. Zhang, Y.; Zhao, Z.; Chen, J.; Cheng, L.; Chang, J.; Sheng, W.; Hu, C.; Cao, S. C-doped hollow TiO₂ spheres: In situ synthesis, controlled shell thickness, and superior visible-light photocatalytic activity. *Appl. Catal. B Environ.* **2015**, *165*, 715–722. [[CrossRef](#)]
55. Guo, L.; Chen, F.; Fan, X.; Cai, W.; Zhang, J. S-doped $\alpha\text{-Fe}_2\text{O}_3$ as a highly active heterogeneous Fenton-like catalyst towards the degradation of acid orange 7 and phenol. *Appl. Catal. B Environ.* **2010**, *96*, 162–168. [[CrossRef](#)]
56. Segal, L.; Creely, J.J.; Martin, A.E.; Conrad, C.M. An Empirical Method for Estimating the Degree of Crystallinity of Native Cellulose Using the X-Ray Diffractometer. *Text. Res. J.* **1959**, *29*, 786–794. [[CrossRef](#)]
57. Bouibes, A.; Zaoui, A. High-pressure phase transitions of forsterite from first-principles. *J. Phys. Chem. Solids* **2020**, *136*, 109161. [[CrossRef](#)]
58. Valencia, E.M.; Worth, C.J.; Fortenberry, R.C. Enstatite (MgSiO₃) and forsterite (Mg₂SiO₄) monomers and dimers: Highly detectable infrared and radioastronomical molecular building blocks. *Mon. Not. R. Astron. Soc.* **2020**, *492*, 276–282. [[CrossRef](#)]
59. Wu, C.Y.; Tu, K.J.; Deng, J.P.; Lo, Y.S.; Wu, C.H. Markedly enhanced surface hydroxyl groups of TiO₂ nanoparticles with Superior water-dispersibility for photocatalysis. *Materials* **2017**, *10*, 566. [[CrossRef](#)] [[PubMed](#)]
60. Pokrovsky, O.S.; Schott, J. Forsterite surface composition in aqueous solutions: A combined potentiometric, electrokinetic, and spectroscopic approach. *Geochim. Cosmochim. Acta* **2000**, *64*, 3299–3312. [[CrossRef](#)]
61. Muir, J.M.R.; Jollands, M.; Zhang, F.; Walker, A.M. Explaining the dependence of M-site diffusion in forsterite on silica activity: A density functional theory approach. *Phys. Chem. Miner.* **2020**, *47*, 1–16. [[CrossRef](#)] [[PubMed](#)]
62. Jeong, H.; Moon, W.; Roh, Y. Characterization of Mineralogical Changes of Chrysotile and its Thermal Decomposition by Heat Treatment. *Econ. Environ. Geol.* **2016**, *49*, 77–88. [[CrossRef](#)]
63. Wang, Y.; Ao, Z.; Sun, H.; Duan, X.; Wang, S. Activation of peroxymonosulfate by carbonaceous oxygen groups: Experimental and density functional theory calculations. *Appl. Catal. B Environ.* **2016**, *198*, 295–302. [[CrossRef](#)]
64. Duan, X.; Ao, Z.; Zhou, L.; Sun, H.; Wang, G.; Wang, S. Occurrence of radical and nonradical pathways from carbocatalysts for aqueous and nonaqueous catalytic oxidation. *Appl. Catal. B Environ.* **2016**, *188*, 98–105. [[CrossRef](#)]
65. Duan, X.; Ao, Z.; Zhang, H.; Saunders, M.; Sun, H.; Shao, Z.; Wang, S. Nanodiamonds in sp²/sp³ configuration for radical to nonradical oxidation: Core-shell layer dependence. *Appl. Catal. B Environ.* **2018**, *222*, 176–181. [[CrossRef](#)]
66. Grebel, J.E.; Pignatello, J.J.; Mitch, W.A. Effect of halide ions and carbonates on organic contaminant degradation by hydroxyl radical-based advanced oxidation processes in saline waters. *Environ. Sci. Technol.* **2010**, *44*, 6822–6828. [[CrossRef](#)] [[PubMed](#)]
67. Yang, Y.; Pignatello, J.J.; Ma, J.; Mitch, W.A. Comparison of halide impacts on the efficiency of contaminant degradation by sulfate and hydroxyl radical-based advanced oxidation processes (AOPs). *Environ. Sci. Technol.* **2014**, *48*, 2344–2351. [[CrossRef](#)]
68. Rivas, F.J.; Solís, R.R. Chloride promoted oxidation of tritosulfuron by peroxymonosulfate. *Chem. Eng. J.* **2018**, *349*, 728–736. [[CrossRef](#)]
69. Luo, R.; Liu, C.; Li, J.; Wang, J.; Hu, X.; Sun, X.; Shen, J.; Han, W.; Wang, L. Nanostructured CoP: An efficient catalyst for degradation of organic pollutants by activating peroxymonosulfate. *J. Hazard. Mater.* **2017**, *329*, 92–101. [[CrossRef](#)]

-
70. Yang, Y.; Jiang, J.; Lu, X.; Ma, J.; Liu, Y. Production of Sulfate Radical and Hydroxyl Radical by Reaction of Ozone with Peroxymonosulfate: A Novel Advanced Oxidation Process. *Environ. Sci. Technol.* **2015**, *49*, 73307339. [[CrossRef](#)]
 71. Khan, S.; He, X.; Khan, J.A.; Khan, H.M.; Boccelli, D.L.; Dionysiou, D.D. Kinetics and mechanism of sulfate radical- and hydroxyl radical-induced degradation of highly chlorinated pesticide lindane in UV/peroxymonosulfate system. *Chem. Eng. J.* **2017**, *318*, 135–142. [[CrossRef](#)]